# Limits on electron neutrino disappearance from the KARMEN and LSND ν_{e}-carbon cross section data

J. M. Conrad and M. H. Shaevitz

Phys. Rev. D **85**, 013017 — Published 23 January 2012

DOI: 10.1103/PhysRevD.85.013017

# Limits on Electron Neutrino Disappearance from the KARMEN and LSND $\nu_e$-Carbon Cross Section Data

J.M. Conrad[1] and M.H. Shaevitz[2]
[1] *Massachusetts Institute of Technology and*
[2] *Columbia University*

This paper presents a combined analysis of the KARMEN and LSND $\nu_e$-carbon cross section measurements within the context of a search for $\nu_e$ disappearance at high $\Delta m^2$. KARMEN and LSND were located at 17.7 m and 29.8 m respectively from the neutrino source, so, the consistency of the two measurements, as a function of antineutrino energy, sets strong limits on neutrino oscillations. Most of the allowed region from the $\nu_e$ disappearance analysis of the Gallium calibration data is excluded at >95% CL and the best fit point is excluded at $3.6\sigma$. Assuming CPT conservation, comparisons are also made to the oscillation analyses of reactor antineutrino data.

PACS numbers: 14.60.Pq,14.60.St

## I. INTRODUCTION

This paper presents an analysis of the $\nu_e$-carbon cross section data from the KARMEN [1] and LSND [2] experiments, within the context of electron neutrino oscillations at high $\Delta m^2$. In a two-neutrino oscillation formalism, the probability for $\nu_e$ disappearance is given by:

$$P = 1 - \sin^2 2\theta \ \sin^2(1.27\Delta m^2(L/E)), \qquad (1)$$

where $\theta$ is the mixing angle; $\Delta m^2 = m_2^2 - m_1^2$, in eV$^2$, is the difference between the squared neutrino masses; $L$, in m, is the distance from the neutrino source to the detector; and $E$, in MeV, is the neutrino energy. This analysis exploits the fact that KARMEN and LSND were located at $L$ =17.7 m and 29.8 m respectively. We use the consistency between the cross section measurements to place strong constraints on $\nu_e$ disappearance at $\Delta m^2 \sim 1$ eV$^2$.

This study is motivated by recent results that can be interpreted as oscillations with $\Delta m^2 \sim 1$ eV$^2$. The strongest evidence comes from the LSND experiment, which observed a $\bar{\nu}_\mu \rightarrow \bar{\nu}_e$ signal corresponding to an oscillation probability of $(0.264 \pm 0.067 \pm 0.045)\%$ [3]. MiniBooNE antineutrino data, published to date [4], are in agreement with LSND, but with less significance, and data continue to be taken to examine how this effect may evolve with higher statistics. The MiniBooNE neutrino data do not support $\nu_\mu \rightarrow \nu_e$ oscillations [5].

High $\Delta m^2$ muon-to-electron flavor appearance cannot be explained in a three neutrino mixing model that also incorporates "solar" and "atmospheric" oscillations [6]. As a result, these data have inspired models with three active and one sterile (3+1) or 2 sterile (3+2) neutrinos. Sterile neutrinos ($\nu_s$) do not interact via the weak interaction, but can mix with and cause oscillations between, the active flavors. These models predict a $\nu_e \rightarrow \nu_s$ signal [7] with a large $\Delta m^2$ (on the order of a few eV$^2$) compared to the splittings between the light states (of order $\sim 10^{-3}$ and $10^{-4}$ eV$^2$). Therefore, one can take the three light states to be effectively degenerate.

This degeneracy simplifies the 3+1 model to an approximate two-neutrino oscillation model for both appearance and disappearance. As a result, Eq. 1 will be applicable to the following discussion, where we will use $\theta_{ee}$ as the mixing angle relevant to $\nu_e$ disappearance.

Recently, a reanalysis of reactor $\bar{\nu}_e$ flux predictions [8] has provoked further interest in electron flavor disappearance in 3+1 models [9–11]. This new analysis resulted in a shift of the ratio of reactor data-to-prediction from $0.976 \pm 0.024$ to $0.943 \pm 0.023$. This deficit with respect to prediction is called the "Reactor Anomaly" in this paper. This can be taken as indication of $\bar{\nu}_e \rightarrow \bar{\nu}_s$ in a 3+1 model at 98.6% CL [9]. The best fit is $\Delta m^2 = 1.78$ eV$^2$ and $\sin^2 2\theta_{ee} = 0.088$ [11].

Indications of $\nu_e$ disappearance have arisen from calibration data taken by the SAGE [12] and GALLEX [13] experiments. These used megacurie sources of $^{51}$Cr and $^{37}$Ar to calibrate the $\nu_e + ^{71}\mathrm{Ga} \rightarrow ^{71}\mathrm{Ge} + e^-$ experiments. The data from SAGE and GALLEX are consistent, and show a measured-to-predicted ratio of $R = 0.86 \pm 0.05$ [10]. We refer to this as the "Gallium data" in this paper. This can be interpreted as a $2.7\sigma$ indication of $\nu_e \rightarrow \nu_s$ oscillations [10, 14]. The best fit in a 3+1 model corresponds to a $\Delta m^2 = 2.24$ eV$^2$ and $\sin^2 2\theta_{ee} = 0.50$ [10]. This apparent $\nu_e$ disappearance signal leads to the argument [15] that $\nu_e \rightarrow \nu_s$, consistent with the Gallium data, must be applied to the intrinsic $\nu_e$ background of the MiniBooNE $\nu_\mu \rightarrow \nu_e$ search [5].

The results of the 3+1 models have provoked substantial interest within the community, but they are not decisive. As a result they are a prime motivation for further studies of electron neutrino disappearance [16, 17].

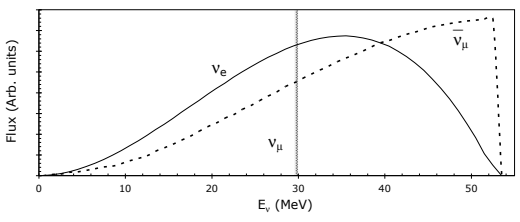


FIG. 1: Energy distribution of neutrinos in a DAR beam.

There are few opportunities for precision $\nu_e$ disappearance searches, since most beams have large uncertainties in the normalization and energy distribution for the $\nu_e$ and $\bar{\nu}_e$ beam contents. However, decay-at-rest (DAR) neutrino beams can provide a unique window on electron-flavor neutrino oscillations.

## II. KARMEN AND LSND

KARMEN and LSND were DAR experiments that ran in the 1990's using 800 MeV protons on target. The isotropic DAR flux, shown in Fig. 1, has equal $\nu_\mu$, $\bar{\nu}_\mu$ and $\nu_e$ content with a well-understood energy spectrum described by weak decay physics. The beam energy extends to 52.8 MeV. The normalization is known to 10%, with the uncertainty dominated by the pion production rate per incident proton [18, 19].

KARMEN ran at the ISIS facility at Rutherford Laboratory, with 200 $\mu$A of protons impinging on a copper, tantalum, or uranium target. The center of the nearly cubic detector was located at 17.7 m from the proton target, at an angle of 100°. The liquid scintillator target volume was 56 m$^3$ and consisted of 512 optically independent modules (17.4 cm × 17.8 cm × 353 cm) wrapped in Gadolinium-doped paper. More details are available in Ref. [20].

LSND used protons from the LAMPF accelerator at Los Alamos National Laboratory (LANL), where a 1 mA beam of protons impinged on a water target. The center of the 8.75 m long, nearly cylindrical detector was located at 29.8 m from the target, at an angle of 12° from the proton beam direction. This was an unsegmented detector with a fiducial mass of 167 tons of oil ($CH_2$), lightly doped with b-PBD scintillator. More details are available in Ref. [21].

Both experiments measured $\nu_e + {}^{12}\mathrm{C} \rightarrow {}^{12}\mathrm{N}_{gs} + e^-$ scattering. In this two-body interaction, with $Q$-value of 17.3 MeV, the neutrino energy can be reconstructed by measuring the outgoing visible energy of the electron. The $^{12}$N ground state is identified by the subsequent $\beta$ decay, ${}^{12}\mathrm{N}_{gs} \rightarrow {}^{12}\mathrm{C} + e^+ + \nu_e$, which has a $Q$-value of 16.3 MeV and a lifetime of 15.9 ms.

## III. THE KARMEN AND LSND CROSS SECTIONS

The KARMEN and LSND cross section measurements for $\nu_e + {}^{12}\mathrm{C} \rightarrow {}^{12}\mathrm{N}_{gs} + e^-$ [1, 2], in energy bins, are compared in Fig. 2. The corresponding flux-averaged cross sections measured by KARMEN and LSND are given in Table I. For completeness, we also list the flux-averaged cross section for the LANL E225 experiment [22], which was located 9 m from a DAR source. (E225 did not publish energy-binned cross section measurements.) The agreement between all three experiments is excellent.

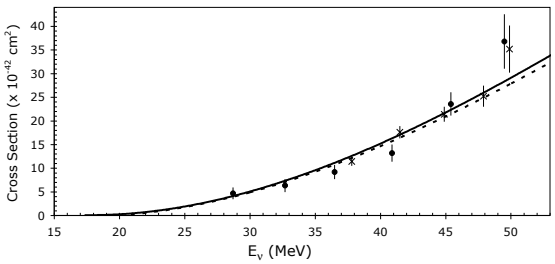


FIG. 2: The KARMEN (points) and LSND (crosses) measured cross sections with statistical errors for $\nu_e + {}^{12}\mathrm{C} \rightarrow {}^{12}\mathrm{N}_{gs} + e^-$ compared to the theoretical prediction of Fukugita, *et al.* (solid line), based on the EPT model, and Kolbe, *et al.* (dashed line), based on the CRPA model.

| Experiment (Dist.) | Flux-Averaged Cross Section | Ref. |
|---|---|---|
| KARMEN (17.7 m) | $(9.1 \pm 0.5 \pm 0.8) \times 10^{-42}$ cm$^2$ | [1] |
| LSND (29.8 m) | $(8.9 \pm 0.3 \pm 0.9) \times 10^{-42}$ cm$^2$ | [2] |
| E225 (9 .0 m) | $(1.05 \pm 0.10 \pm 0.10) \times 10^{-41}$ cm$^2$ | [22] |
| **Prediction** | **Flux-Averaged Cross Section** | **Ref.** |
| Fukugita *et al.* | $9.2 \times 10^{-42}$ cm$^2$ | [23] |
| Mintz *et al.* | $8.0 \times 10^{-42}$ cm$^2$ | [25] |
| Donnelly | $9.4 \times 10^{-42}$ cm$^2$ | [24] |
| Kolbe *et al.* | $8.9 \times 10^{-42}$ cm$^2$ | [26] |

TABLE I: Top: Flux-averaged $\nu_e + {}^{12}\mathrm{C} \rightarrow e^+ + {}^{12}\mathrm{N}_{gs}$ cross section measurements with statistical and systematic error. Bottom: Flux-averaged predictions from EPT (Fukugita, Mintz and Donnelly) and CRPA (Kolbe) models. Flux-average cross section values are equivalent to those for a neutrino of 35 MeV energy.

The measured cross sections are compared to predictions by Fukugita, *et al.*[23] and by Kolbe *et al.*[26] in Fig. 2. Both models follow an $(E_\nu - Q)^2$ form, where $Q = 17.3$ MeV. This energy dependence arises because the interaction is an allowed transition, converting the $0^+$ ($^{12}$C) state to the $1^+$ ($^{12}$N) state. The Fukugita prediction is calculated within the "elementary particle model" (EPT) and has an associated 12% normalization uncertainty [23]. Other EPT predictions, include Donnelly [24] and Mintz, *et al.*, are given in Table I. For comparison, the Kolbe, *et al.*, calculation [26] is performed within a "continuum random phase approximation" (CRPA) approach. A discussion of the relative merits of EPT versus CRPA models for describing this process appears in Ref. [27]. From a strictly experimental point of view, both EPT and CRPA models fit the data well. To be clear, these theoretical results are true predictions rather than fits, since they were published well before the KARMEN and LSND results.

## IV. CONSTRAINTS ON ELECTRON NEUTRINO DISAPPEARANCE

The allowed regions for $\nu_e \rightarrow \nu_s$ oscillations are determined from a comparison of the LSND and KARMEN

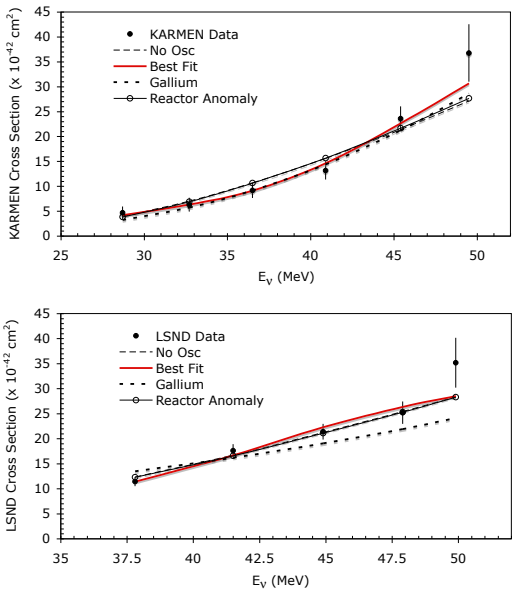


FIG. 3: Comparisons of the data to various oscillation predictions for the LSND (top) and KARMEN (bottom) data using the Fukugita prediction, as described in the text.

data with respect to the Fukugita prediction. For a given oscillation hypothesis ($\Delta m^2$ and $\sin^2 2\theta_{ee}$), we calculate a combined $\chi^2$ for LSND and KARMEN with respect to the prediction using the statistical error for each data point and employing three pull terms as a method to incorporate systematic uncertainties. The first pull term represents the correlated normalization error. As noted in the KARMEN paper [1], LSND and KARMEN have a 7% systematic error on the neutrino flux normalization from the flux simulation that is correlated between the two experiments [18, 19]. This is combined in quadrature with the 12% systematic error on the normalization for the Fukugita prediction to give the correlated normalization pull term in the $\chi^2$ calculation. The remaining uncorrelated normalization uncertainties for each experiment are 7% for LSND [2] and 5% for KARMEN [1]. These uncertainties are used as the two other pull terms in the $\chi^2$ calculation. To determine the 90% CL allowed regions in $\Delta m^2$ and $\sin^2 2\theta_{ee}$, we marginalize over the three normalization pull parameters and use a $\Delta\chi^2 > 4.61$ requirement for the two-degrees-of-freedom excluded region.

The results of the fits using the Fukugita prediction are shown in Fig. 3. Table II reports the $\chi^2$ and degrees of freedom (DOF) for various joint fits to the LSND and KARMEN data points. The fit without oscillations (No Osc), shown as the long-dashed line in Fig. 3, has a $\Delta\chi^2$ probability of 91.5% and is only excluded at the $1.7\sigma$ level. As a result, we use the data to set a limit on $\nu_e$ disappearance and calculate the 95% CL exclusion region shown in Fig. 4. The best fit, indicated by the solid lines in Fig. 3, is at $\Delta m^2 = 7.49 \pm 0.39$ eV$^2$ and $\sin^2 2\theta_{ee} = 0.290 \pm 0.115$.

Comparing the data to an oscillation model with the best-fit Gallium parameters illustrates the disagreement, though we note that the Gallium fit had a rather shallow minimum [10, 14]. The Gallium fit reported in Table II and shown as the dashed line on Fig. 3 is poor. This point has a $\chi^2$ probability of less than $3.2 \times 10^{-4}$ and is, therefore, ruled out at $3.6\sigma$. (The $\Delta\chi^2$ for this point has a probability of $5.3 \times 10^{-7}$, which corresponds to a $5.0\sigma$ exclusion.) Most of the Gallium allowed region, indicated at 68% and 90% CL on Fig. 4, is excluded at 95% CL by this analysis.

As discussed above, all models tend to follow a ($E_\nu -$

Fukugita et al. Cross Section

| Fit Type | $\Delta m^2$(eV$^2$) | $\sin^2 2\theta_{ee}$ | $\chi^2$/DOF |
|---|---|---|---|
| Best Fit | 7.49 ± 0.39 | 0.290 ±0.115 | 5.5/9 |
| No Osc | — | 0.000 (fixed) | 10.4/11 |
| Gallium | 2.24 (fixed) | 0.500 (fixed) | 34.3/11 |
| Reactor Anomaly | 1.78 (fixed) | 0.089 (fixed) | 10.2/11 |

Kolbe et al. Cross Section

| Fit Type | $\Delta m^2$(eV$^2$) | $\sin^2 2\theta_{ee}$ | $\chi^2$/DOF |
|---|---|---|---|
| Best Fit | 7.49 ± 0.39 | 0.281 ± 0.115 | 6.1/9 |
| No Osc | — | 0.000 (fixed) | 10.7/11 |
| Gallium | 2.24 (fixed) | 0.500 (fixed) | 37.8/11 |
| Reactor Anomaly | 1.78 (fixed) | 0.089 (fixed) | 10.8/11 |

TABLE II: Results of fits using the Fukugita (top) or Kolbe (bottom) cross sections for the predicted energy dependence. The resultant or assumed $\Delta m^2$ and $\sin^2 2\theta_{ee}$ values, along with the $\chi^2$ and degrees of freedom (DOF) for the fits are shown.

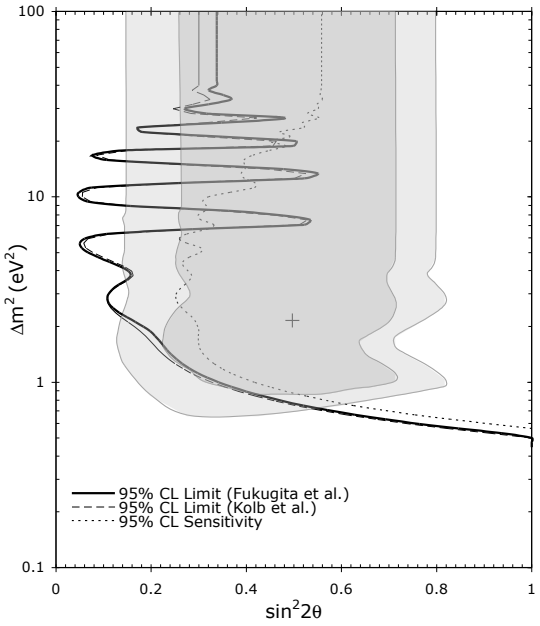


FIG. 4: The 95% $\nu_e$ disappearance limit from the Fukugita (EPT) fit (solid, black line) compared to the predicted sensitivity (dotted line). Also shown is the 68% (darker, shaded region) and 90% (lighter, shaded region) contours from the Gallium experiments. The dashed line is the Kolbe (CRPA) fit.

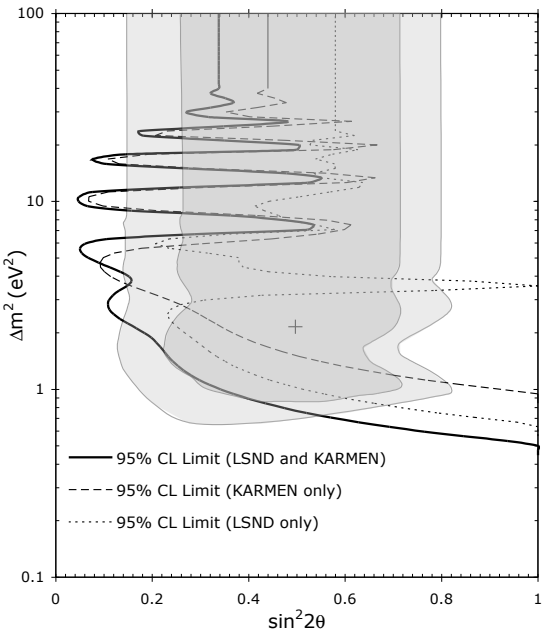


FIG. 5: The 95% $\nu_e$ disappearance limit from the combined fit (solid, black line) compared to individual fits to KARMEN data (dashed) and LSND data (dotted). This is overlaid on the Gallium 90% and 68% CL allowed regions. All fits use the Fukugita model.

$Q)^2$ dependence. Nevertheless, small differences between the Fukugita (EPT) and Kolbe (CRPA) predictions, shown in Fig. 2, allow a test for model dependence. The Kolbe fit proceeds in the same way as for the Fukugita model. The resulting $\chi^2$ values for the fits are given in Table II. The comparisons of the fits with the data are indistinguishable from those shown in Fig. 3 and so are not shown here. This leads to the conclusion that there is no substantial systematic effect from the energy dependence of the underlying cross section model. The 95% CL exclusion limit from the Kolbe fit is also shown in Fig. 4 as the dashed contour and is very similar to the Fukugita contour.

The excluded region in Fig. 4 is better than the expected sensitivity region (dotted contour) calculated for an underlying null oscillation hypothesis. As a way of quantifying this difference, using the Fukugita model fit, the Gallium data point is ruled out in a $\chi^2$ analysis at $3.6\sigma$, while the sensitivity would have predicted that, for an average experiment with no signal, the Gallium point would be ruled out at $2.8\sigma$. This strong limit with respect to the sensitivity is not unlikely; we find that 11% of simulated experiments have a high $\Delta m^2$ 95% CL limit for $\sin^2 2\theta_{ee}$ at or below the 0.34 95% CL limit of this analysis. These studies also show that $\Delta\chi^2$ is a good statistic for determining the exclusion regions since 10% of the simulated experiments have a $\Delta\chi^2$ value for the null oscillation hypothesis greater than 4.61 as expected for two degrees of freedom.

The combined fit to KARMEN and LSND is stronger than fits to the the individual data sets because the detectors are at different distances. Requiring the proper $L$ as well as $E$ dependence adds an important constraint to the oscillation fit. The results of the individual fits are compared to the combined fit in Fig. 5. A fit to only the KARMEN data yields a best fit $\chi^2$ of 2.46 for 4 degrees of freedom, with the parameters $\sin^2 2\theta = 0.333 \pm 0.130$ and $\Delta m^2 = 7.54$ eV$^2$. The $\chi^2$ for the null fit was 7.05 for 6 degrees of freedom. A fit to only the LSND data results in a best fit $\chi^2$ of 2.27 for 3 degrees of freedom, with the parameters $\sin^2 2\theta = 0.209 \pm 0.331$ and $\Delta m^2 = 3.90$ eV$^2$. The $\chi^2$ for the null fit was 3.29 for 5 degrees of freedom.

Considering fits to these two data sets separately allows interpretation of certain features in the combined fit. We see in Fig. 5 that the KARMEN data dominates at high $\Delta m^2$ because of statistics and that the large variations in the limit are driven by this data set. These variations appear because the event energy distribution spans a limited range. As a result, there are oscillation parameters for which the KARMEN distance allows the experiment to either be very sensitive or very insensitive to disappearance. The LSND data set allows full oscillation at $\Delta m^2$ of 3.9 eV$^2$, but KARMEN data does not. At low $\Delta m^2$, the sensitivity is dominated by the LSND data although the combination with KARMEN is significantly better.

## V. BROADER INTERPRETATION OF THIS CONSTRAINT

The limit presented here and the Gallium data represent the only electron neutrino disappearance results in this $\Delta m^2$ range. Comparison to other data sets require interpretation within models. Specific global analyses are beyond the scope of this paper, however, we can consider the impact of the limit, in general.

CPT conservation requires that $\nu_e$ and $\bar{\nu}_e$ disappearance should occur at the same rate. Because CPT conservation is embedded in all field theories, comparison of electron flavor neutrino and antineutrino disappearance is widely regarded as interesting. The relavent antineutrino disappearance data comes from the reactor experiments. The recently published Reactor Anomaly hints at oscillations, and the parameters from the $\bar{\nu}_e$ disappearance data [9] can be compared to the $\nu_e$ results assuming CPT conserving models.

In Fig. 6, we overlay the Reactor Anomaly allowed region at 68% and 90% CL with the 95% CL limit from this paper using Fukugita. In this figure, we use a log scale for $\sin^2 2\theta$ so that the reactor allowed region is clear. One can see that portions of the allowed reactor space will be excluded in fits that require CPT conservation. However, the Reactor Anomaly best fit parameters give a $\Delta\chi^2$ probability of 90.8%, which lies outside of the 95% CL excluded region from the cross section analysis limit, and one expects portions of the allowed region to survive in a global fit. The comparison of the best fit with data,

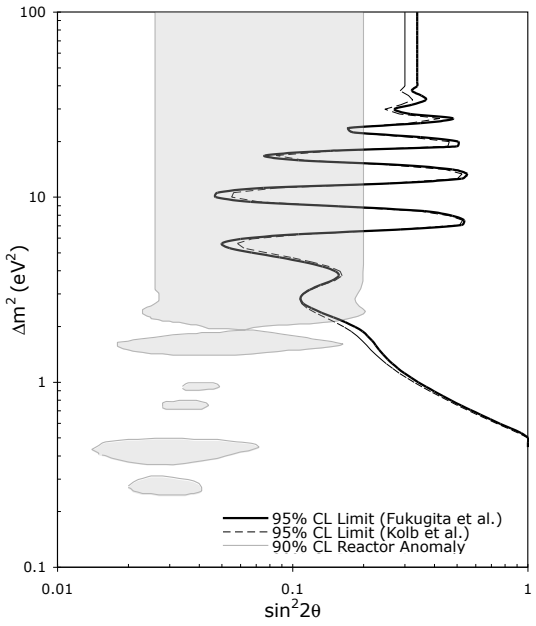


FIG. 6: The 95% $\nu_e$ disappearance limit from the Fukugita (EPT) fit (solid, black line) and Kolbe (CRPA) fit compared to the 90% (shaded region) contours from the Reactor Anomaly.

shown as the thin line with dots in Fig. 3, is reasonably good and similar to the "no oscillation" case, illustrating why the KARMEN/LSND data does not speak to the entire region of the Reactor Anomaly. This is consistent with good the $\chi^2$/DOF for the best fit point of the reactor anomaly, reported in Table II.

Comparisons to electron-to-muon flavor appearance data is much more model dependent than the comparison of $\bar{\nu}_e$ to $\nu_e$ disappearance. In this case, one must go beyond choosing whether or not to assume CPT conservation, to include the number of sterile neutrinos (typically, one assumes 3+1 or 3+2 models); the mass heirarchy (a 1+3+1 model has recently been published [11] as a variation of the two sterile neutrino case); and whether or not to include CP violation.

Inclusion of the appearance data also, necessarily, requires reference to muon-flavor disappearance as well as electron flavor disappearance, since these are all realted. As an example, in a 3+1 model:

$$\sin^2 2\theta_{\mu e} = 4U_{e4}^2 U_{\mu 4}^2, \quad (2)$$

$$\sin^2 2\theta_{\mu\mu} = 4U_{\mu 4}^2(1 - U_{\mu 4}^2), \quad (3)$$

$$\sin^2 2\theta_{ee} = 4U_{e4}^2(1 - U_{e4}^2); \quad (4)$$

where $U_{\alpha i}$ represents the element in the 4-neutrino mixing matrix. The disappearance limit we present here, when interpreted within Eq. 4, substantially limits the range of $U_{e4}^2$, and will considerably reduce the space of allowed values for matrix elements that can describe muon-to-electron flavor appearance in neutrino mode, as may be implied by the MiniBooNE low energy excess [5]. While the correspondences between experimentally measured mixing angles and the underlying matrix elements for two-sterile-neutrino models is more complicated, the basic point still applies.

## VI. CONCLUSIONS

This analysis has used the $\nu_e + {}^{12}\mathrm{C} \rightarrow {}^{12}\mathrm{N}_{gs} + e^-$ cross section data from LSND and KARMEN to constrain the amount of $\nu_e$ disappearance oscillations at high $\Delta m^2$. The good agreement between the data sets and with the theory, despite different distances of detectors from the source, leads to an 95% CL exclusion region which extends down to $\sin^2 2\theta_{ee} = 0.34$ at high $\Delta m^2$ and to considerably lower values for some $\Delta m^2$ ranges. Comparison to another underlying cross section model does not significantly change the excluded region.

The data are in disagreement with the only other $\nu_e$ disappearance data set in this $\Delta m^2$ region, which comes from the Gallium experiments. Large portions of the allowed region for $\nu_e$ disappearance analysis of the Gallium calibration data are ruled out at >95% CL. As a benchmark, the best fit point for Gallium is excluded at $3.6\sigma$. This new limit also severely restricts models addressing the MiniBooNE results, such as Ref. [15], that incorporate $\nu_e$ disappearance to explain the observed energy distribution.

Assuming CPT conservation, this data set can be compared to the $\bar{\nu}_e$ disappearance from reactor data. The Reactor Anomaly best fit point in this case is within the allowed 95% CL contour but some regions of the allowed region in Ref. [9] are excluded.

### Acknowledgments

The authors thank the National Science Foundation for support.

[1] B. E. Bodmann *et al.* [KARMEN Collaboration.], Phys. Lett. B **332**, 251 (1994). B. Armbruster, *et al.* [KARMEN Collaboration], Phys. Rev. C57, 3414 (1998).
[2] L. B. Auerbach *et al.* [LSND Collaboration], Phys. Rev. C **64**, 065501 (2001).
[3] A. Aguilar *et al.* [LSND Collaboration], Phys. Rev. D **64**, 112007 (2001).
[4] A. A. Aguilar-Arevalo *et al.* [The MiniBooNE Collabo-

ration], Phys. Rev. Lett. **105**, 181801 (2010).
[5] A. A. Aguilar-Arevalo *et al.* [The MiniBooNE Collaboration], Phys. Rev. Lett. **98**, 231801 (2007).
[6] M. Sorel, J. M. Conrad and M. Shaevitz, Phys. Rev. D **70**, 073004 (2004).
[7] G. Karagiorgi, Z. Djurcic, J. M. Conrad, M. H. Shaevitz and M. Sorel, Phys. Rev. D **80**, 073001 (2009) [Erratum-ibid. D **81**, 039902 (2010)].
[8] T. A. Mueller *et al.*, Phys. Rev. C **83**, 054615 (2011).
[9] G. Mention, M. Fechner, T. Lasserre, T. A. Mueller, D. Lhuillier, M. Cribier and A. Letourneau, Phys. Rev. D **83**, 073006 (2011).
[10] C. Giunti and M. Laveder, Phys. Rev. C **83**, 065504 (2011)
[11] J. Kopp, M. Maltoni and T. Schwetz, arXiv:1103.4570 [hep-ph], see Table 1, where $\sin^2 2\theta_{ee} = 4|U_{e4}|^2(1 - |Ue4|^2)$, taking $|U_{\mu 4}|^2$ and $|U_{\tau 4}|^2$ to be negligible.
[12] J. N. Abdurashitov *et al.* [SAGE Collaboration], Phys. Rev. C **80**, 015807 (2009).
[13] F. Kaether, W. Hampel, G. Heusser, J. Kiko and T. Kirsten, Phys. Lett. B **685**, 47 (2010).
[14] M. A. Acero, C. Giunti and M. Laveder, Phys. Rev. D **78**, 073009 (2008).
[15] C. Giunti and M. Laveder, Phys. Rev. D **82**, 053005 (2010).
[16] S. K. Agarwalla, J. M. Conrad and M. H. Shaevitz, arXiv:1105.4984 [hep-ph].
[17] A. Palazzo, Phys. Rev. D **83**, 113013 (2011)
[18] R. L. Burman, Nucl. Instrum. Meth. A **368**, 416 (1996).
[19] R. L. Burman, M. E. Potter and E. S. Smith, Nucl. Instrum. Meth. A **291**, 621 (1990).
[20] G. Drexlin, *et al.*, Nucl. Instr. and Meth., A **289** 490 (1990).
[21] C. Athanassopoulos, *et al.*, "The Liquid Scintillator Neutrino Detector and LAMPF Neutrino Source," Nucl. Instr. Meth. A 388: 149 (1997).
[22] D. A. Krakauer, *et al.*, Phys. Rev. C **45**, 2450 (1992).
[23] M. Fukugita, Y. Kohyama and K. Kubodera, Phys. Lett. B **212**, 139 (1988).
[24] T. W. Donnelly and R. D. Peccei, Phys. Rept. **50**, 1 (1979).
[25] S. L. Mintz and M. Pourkaviani, Phys. Rev. C **37**, 2249 (1988).
[26] E. Kolbe, K. Langanke, and P. Vogel, Nucl. Phys. A **652**, 91 (1999).
[27] E. Kolbe, K. Langanke, and P. Vogel, Nucl. Phys. A **613**, 382 (1999).